Published in final edited form as:
Neuroimage. 2012 April 15; 60(3): 1856–1866. doi:10.1016/j.neuroimage.2012.01.132.

Deficits in axonal transport in hippocampal-based circuitry and the visual pathway in APP knock-out animals witnessed by manganese enhanced MRI

Joseph J. Gallagher[1,*], **Xiaowei Zhang**[1], **Greg Ziomek**[2], **Russell E. Jacobs**[1], and **Elaine L. Bearer**[1,2]

[1]Biological Imaging Center, Beckman Institute, m/c 139-74, California Institute of Technology, Pasadena, California, 91125, United States of America

[2]Department of Pathology, University of New Mexico Health Sciences Center, Albuquerque, New Mexico, 87131 United States of America

Abstract

Mounting evidence implicates axonal transport defects, typified by the presence of axonal varicosities with aberrant accumulations of cargo, as an early event in Alzheimer's disease (AD) pathogenesis. Work identifying amyloid precursor protein (APP) as a vesicular motor receptor for anterograde axonal transport further implicates axonal transport in AD. Manganese-enhanced MRI (MEMRI) detects axonal transport dynamics in preclinical studies. Here we pursue an understanding of the role of APP in axonal transport in the central nervous system by applying MEMRI to hippocampal circuitry and to the visual pathway in living mice homozygous for either wild type or a deletion in the APP gene (n = 12 for each genotype). Following intra-ocular or stereotaxic hippocampal injection, we performed time-lapse MRI to detect Mn^{2+} transport. Three dimensional whole brain datasets were compared on a voxel-wise basis using within-group pair-wise analysis. Quantification of transport to structures connected to injection sites via axonal fiber tracts was also performed. Histology confirmed consistent placement of hippocampal injections and no observable difference in glial-response to the injections. APP −/− mice had significantly reduced transport from the hippocampus to the septal nuclei and amygdala after 7 hours and reduced transport to the contralateral hippocampus after 25 hours; axonal transport deficits in the APP −/− animals were also identified in the visual pathway. These data support a system-wide role for APP in axonal transport within the central nervous system and demonstrate the power of MEMRI for assessing neuronal circuitry involved in memory and learning.

Keywords

Amyloid precursor protein; Manganese enhanced MRI (MEMRI); Alzheimer's disease; axonal transport; statistical parametric mapping; optic tract; synaptic transmission; hippocampus; visual pathway

[*]Corresponding Author: Biological Imaging Center, Beckman Institute, m/c 139-74, California Institute of Technology, Pasadena, California, United States of America. jjg@caltech.edu Phone: 1-626-395-2004. Fax: 626-449-5163.

Introduction

Alzheimer's disease (AD) is characterized by progressive neuronal and synaptic dysfunction and loss. Progressive deficits in episodic memory ultimately lead to marked dementia, evidenced by loss of short-term memory, impaired judgement, altered behaviour, and general decline in cognitive function (Keller, 2006). The pathological hallmarks of AD are senile plaques and neurofibrillary tangles (NFTs); both of which involve proteins implicated in axonal transport. Mounting evidence implicates axonal transport defects, typified by the presence of axonal varicosities with aberrant accumulations of cargo, as an early event in AD pathogenesis (Stokin et al., 2005).

Senile plaques are lesions comprised of a core of aggregated amyloid-β (Aβ) surrounded by reactive astrocytes, dystrophic neurites and activated microglia (Ishihara et al., 1991). Aβ, the main constituent of senile plaques, is derived from the proteolytic cleavage of the amyloid precursor protein (APP), a type I, 695 – 770 residue, glycosylated transmembrane protein with a large hydrophilic extracellular domain, a hydrophobic 23 residue transmembrane domain and a short, 47 residue, cytoplasmic domain (Walsh and Selkoe, 2007). The normal physiological role of APP is unclear but several functions have been proposed, including roles in axonal transport, cell adhesion, copper homeostasis and neuronal migration during development (Heber et al., 2000; Herms et al., 2004; Kamal et al., 2001; Muller et al., 1994; Satpute-Krishnan et al., 2006; Young-Pearse et al., 2007). Studies in APP knock-out mice (APP−/−) also identify impaired hippocampal long-term potentiation (LTP) and deficits in passive avoidance learning (Dawson et al., 1999; Senechal et al., 2008).

The identification of APP as a vesicular motor receptor for anterograde axonal transport machinery links axonal transport to the senile plaques observed in AD. Various transgenic animal models have proven valuable for discovery of this physiological role of APP (Price et al., 2000). For example, deletion of the *Drosophila* homolog of APP results in anterograde transport defects similar to those produced by a kinesin light chain (KLC) knock-out (Gunawardena and Goldstein, 2001; Torroja et al., 1999). Similarly, deletion of APP in mice results in a reduction in anterograde transport of kinesin-1 cargo (Kamal et al., 2001), possibly mediated by binding of the cytoplasmic domain of APP to kinesin-1 light chains (Kamal et al., 2000); whether transport is mediated through direct binding between APP and KLC remains controversial (Lazarov et al., 2005). Subsequently, a short peptide sequence (15 aa) derived from the cytoplasmic C-terminus of APP was found to be sufficient for anterograde transport of exogenous cargo in the giant axon of the squid (Satpute-Krishnan et al., 2006). More recent work reported the travel of endogenous APP cleavage products to specific cellular destinations and noted this segregation was abolished upon APP overexpression, indicating an increasingly complex system (Muresan et al., 2009). Histological evidence indicative of defective axonal transport has also been reported in a variety of mouse models of AD that over-express mutant forms of APP, Presenilin-1 and/or tau (Stokin et al., 2005; Wirths et al., 2006). Taken together these observations suggest APP and its metabolites are connected to axonal transport mechanisms and that manipulation of APP would lead to axonal transport deficits (Shah et al., 2009).

Manganese-enhanced magnetic resonance imaging (MEMRI) enables *in vivo* assessment of axonal transport due to three properties of Mn^{2+}: its paramagnetism leads to alterations in T_1 relaxation time, producing a hyper-intense signal in T_1-weighted MR images; as a calcium-analogue Mn^{2+} enters neurons via calcium channels; and, once inside neurons, Mn^{2+} is transported via fast axonal transport (Bearer et al., 2009; Lin and Koretsky, 1997; Merritt et al., 1989; Pautler, 2004; Silva et al., 2004; Zhang et al., 2010). MEMRI protocols detecting axonal transport have identified deficits in aged rats (Cross et al., 2008) and in mouse

models of AD (Kim et al., 2011; Smith et al., 2007; Smith et al., 2011). *In vivo* assessment has predominantly focused on axonal transport in the fascicles of the olfactory bulbs and recent work identified a deficit in olfactory bulb axonal transport in APP −/− mice (Smith et al., 2010). Bearer and colleagues, 2007, identified a dependence for Mn^{2+} transport on kinesin light chain 1, a subunit of the kinesin-1 motor protein (Bearer et al., 2007a). Thus Mn^{2+} transport detected by time-lapse MRI is a reliable biomarker for microtubule-based axonal transport within the living brain.

Here, we exploit MEMRI to assess axonal transport dynamics between the hippocampus and other brain regions - the septal nuclei of the basal forebrain, amygdala, and contralateral hippocampus - in mice with and without the APP gene; and in separate experiments we also assess axonal transport dynamics in the visual pathway from retina to brain. Successive MR images of the same animal acquired over time after Mn^{2+} injection allow us to follow Mn^{2+}-induced hyperintensity progressing along well-established fiber tracts composed of axonal bundles. After rigorous investigation of injection site locations and possible confounding factors due to APP absence, such as microglial activation and volumetric alterations in APP −/− mouse brains, statistical parametric analysis revealed deficits in axonal transport in the central nervous system of APP−/− animals.

Methods

Animals

Mice were obtained from Jackson Laboratories (Stock number 004133, Bar Harbor, ME), 12 female APP −/− and 12 wild type controls hereafter referred to as APP −/− and wild type respectively, were used in this study. APP −/− mice were designed on a C57BL/6J background lacking the promoter and first exon of APP as previously described (Zheng et al., 1995) and as used in a study identifying transport deficits in the olfactory system via MEMRI (Smith et al., 2010). Animals were between 4 – 5 months of age at the time of experiments and genotypes were confirmed by PCR at JAX according to their standard protocols. APP−/− mice were smaller than wild type and this finding extended to the brain. However, structural abnormalities in the hippocampal commissures reported for other strains of APP deficient mice (Magara et al., 1999) were not present in the strain used in this study (Supplemental Fig. 1a,b). All protocols involving animals in this work were approved by both the Institutional Animal Care and Use Committee (IACUC) of the California Institute of Technology and the University of New Mexico IACUC committee.

Intra-ocular Manganese Injections

Mice were anesthetized using 1.5 % isoflurane, placed into a stereotaxic frame (Kopf Instruments, CA, USA) and maintained under anesthesia throughout intra-ocular Mn^{2+} administration. A fine steel needle (30 gauge, 0.3 mm) was used to bore into the sclera. Upon removal of the needle, a catheter tip (Tail-vein catheter, SAI Inc., IL, USA) was introduced into the eye. Mn^{2+} (250 nl, 200 mM; prepared with deionized water in sterile saline) was injected behind the lens into the vitreous of the right eye over the course of a minute, the catheter was slowly removed and the animal transferred to the MR scanner and maintained under anesthesia with 1 – 1.5 % isoflurane in medical grade air during a scan to confirm Mn^{2+} presence in the eyeball (Bearer et al., 2007a). Animal respiration and chamber temperature were monitored during scanning.

Stereotaxic Hippocampal Injections

The stereotaxic injection procedure was similar to that employed by Bearer et al, 2007 (Bearer et al., 2007b). Briefly 5 nl of 500 mM Mn^{2+}, prepared with deionized water, was injected unilaterally into the right hippocampus (coordinates $x = -3.2$ mm (midline), $y =$

−4.1 mm (bregma), *z* =3.4 mm (down) (Paxinos, 2001)) over 5 minutes using a quartz micropipette guided by computer-assisted stereotaxic injector (myNeuroLab.com, IL, USA). All mice also received 0.5 mg/ml rhodamine dextran-amine (RDA; 3k; Molecular Probes/ Invitrogen, OR, USA) during Mn^{2+} administration. Following micropipette removal, animals were transferred to the scanner and maintained under anesthesia with 1 – 1.5 % isoflurane in medical grade air. Inspection of MR images obtained 1 hour after injection enabled identification of a hypointense region representing the injection site. The coordinates of this region were identified in all animals and translated to the bregma coordinate system by applying the transformation required to align the coordinates of the anterior commissure in the 1 hour MR images and the high resolution template image used throughout the study.

Magnetic Resonance Imaging

All animals were imaged prior to administration of Mn^{2+} to acquire a pre-injection image. Mice received 0.3 ml of saline subcutaneously before each imaging session and protective eye ointment was applied to protect eyes from damage (Puralube, Pharmaderm, NY). Animals receiving hippocampal injections were imaged at 0:54 ± 0:15, 6:41 ± 0:11 and 24:43 ± 0:23 hours post injection. Animals receiving intra-ocular injections were imaged 1 hour after injection to check that the injection was successful; the increased T1 weighted signal intensity confirmed the presence of Mn^{2+} in the globe. These animals were then returned to their cages and imaged 25:14 ± 0:45 hours later. No significant differences existed in the times for experimental groups. The midpoint of each 46 minute scan was identified as the “scan time” and in the case of the hippocampal injections will be referred to as occurring 1, 7, and 25 hours after Mn^{2+} injection. Imaging following intra-ocular injection will be referred to as 25 hours after injection. Both procedures were performed on the same group of mice, with intra-ocular experiments performed at minimum 14 days prior to the hippocampal experiments in all instances. Previous experimental observations from this laboratory indicated this was sufficient to ensure Mn^{2+} clearance (Zhang and Jacobs, unpublished observations). Further validation that this wait time eliminated contaminating intensities from the eye injection is evidenced by the absence of signal increase in visual pathways in the hippocampal injection analyses.

An 11.7 T 89 mm vertical bore Bruker BioSpin Avance DRX500 scanner (Bruker BioSpin Inc., Billerica, MA) equipped with a Micro 2.5 gradient system was used to acquire all mouse brain images with a 35 mm linear birdcage radio frequency (RF) coil. During imaging the animal's head was secured in a Teflon stereotaxic unit within the RF coil to minimize movement and to aid in reproducible placement. Temperature and respiration were continuously monitored during data acquisition and remained within normal ranges. Similar to previous MEMRI studies carried out by this group (Hennig et al., 1986), we employed a 3D RARE imaging sequence with RARE factor of 4 and the following parameters: 4 averages, TR/TE_{eff} = 250 ms/12 ms; matrix size of 160×128×88; FOV 16 mm × 12.8 mm × 8.8 mm; yielding 100 μm isotropic voxels with a 46 minute scan time.

Fixation for Histology and Diffusion Tensor Imaging

Mice were sacrificed 9 – 10 days after the final MR imaging session. Each mouse was anaesthetized and perfused with warm heparinized phosphate buffered saline (PBS; 30 ml) followed by 30 ml of room temperature 4 % paraformaldehyde (PFA) in PBS. Following decapitation the head was rocked in 4 % PFA in PBS overnight at 4 °C. Samples intended for *ex vivo* MRI were kept within the skull, had all skin and cartilaginous tissue removed and were maintained at 4 °C in 0.01 % sodium azide in PBS before further processing prior to scanning.

Diffusion-Weighted MRI

Two intact heads prepared as described above were secured in a Teflon® holder and submerged in perfluoropolyether (Fomblin®, Solvay Solexis, Inc., Thorofare, NJ) within a 50 ml vial and imaged at 4°C. Diffusion weighted images (DWI) were acquired using a conventional pulsed-gradient spin echo (PGSE) sequence (TR/TE = 300 ms/11.9 ms, 256×150×120 matrix, 25.6 mm ×15 mm ×12 mm FOV, 100 μm isotropic voxel size, 1 average, δ = 3 ms, Δ = 5.2 ms, G_d = 1125 mT/m, nominal b-factor = 3370 s/mm^2). An optimized six point icosahedral encoding scheme (Hasan et al., 2001) was used for diffusion weighted acquisitions with a single un-weighted reference image for a total imaging time of 14.5 hours. Fractional Anisotropy (FA) maps were calculated and regions of interest (ROI) were manually drawn on the dorsal hippocampal commissure and corpus callosum (combined) and the ventral hippocampal commissure to determine an average fractional anisotropy (FA) for both groups. Results are presented in Supplementary Fig. 1a.

Histology

Histological examination was performed on 8 brains, 4 APP −/− and 4 wild type. Prior to processing, each brain was released from the skull, post-fixed for 1 – 3 days and sent to Neuroscience Associates (NSA, TN, USA) for gelatin embedding and frozen sectioning as described (Bearer et al., 2009). Brains were embedded in a single gelatin block and sectioned in register at 30 μm thickness. Every 12th section was stained with a Solochrome technique, developed for this study in collaboration with NSA, and an adjacent section mounted in DAPI-containing anti-quench and mounted for fluorescence microscopy of the co-injected rhodamine-dextran. Microglial activation was assessed by inspection of sections stained by indirect immunohistochemistry for ionized calcium binding adaptor molecule 1 (Iba1). Cholinergic neurons were detected by immunohistochemistry for choline acetyltransferase (ChAT) (Bearer et al., 2007b). Microscopy of whole brain sections was performed using a Zeiss V8 stereoscope equipped with an Axiocam running AxioVision 4.8, bright and dark-field illumination and three fluorescent filter cubes for DAPI, TRITC, and FITC. High magnification assessment of rhodamine-dextran and DAPI at the injection site, the septal nuclei in the forebrain and the contralateral hippocampus were obtained on a Zeiss Axioscope Z1 with an MRM and HRC Axiocam running AxioVision 4.6 software. Microscopy images were prepared for publication figures using Adobe Photoshop.

MR Image Alignment and Pre-Processing

MR images were skull-stripped using the Brain Surface Extractor within BrainSuite9 (Shattuck and Leahy, 2001) and the Extract Brain Surface tool in MIPAV (Biomedical Research and Services Section, 2011). Inaccuracies were corrected by manual revision of the masks in either image processing tool. Statistical parametric mapping (SPM) analysis was completed in a similar fashion to previous MEMRI studies published by our group (Bearer et al., 2007b; Bearer et al., 2009; Zhang et al., 2010). Briefly, after skull-stripping, each image was scaled to the mode of its intensity histogram. A high-resolution *in vivo* MR image of a wild type mouse (80 μm isotropic; 145×180×88 matrix; RARE) obtained 24 hours following intraperitoneal administration of Mn^{2+} (0.4 mM/kg in 0.4 ml saline), providing excellent contrast of brain structures normally unidentifiable (Aoki et al., 2004), was utilized as the template image in this study; such that all images acquired in this study were co-registered to this image as described below. With reference to the Paxinos and Watson Mouse Brain Atlas (Paxinos, 2001), brain regions identifiable and relevant to this study (e.g. hippocampus, superior colliculus) were segmented on this template image; enabling visualization of injection sites and SPM results with respect to relevant brain regions. The segmented anatomical regions were also used to identify the number of statistically significant voxels in specific anatomical regions.

All pre-injection images obtained in this study were registered to the template image using a 12-parameter full-affine model. The resulting transformation was used as input for the transformation of the post-injection images to the template using Alignlinear, following initial linear alignment (12 parameter model) using the LONI Pipeline Processing Environment (Rex et al., 2003). Group-specific average images were created to enable visual assessment of signal enhancement due to Mn^{2+} presence and transport following intra-hippocampal and intra-ocular Mn^{2+} administration. Final images were prepared for SPM analysis through application of 0.3 mm Gaussian kernel.

Statistical Parametric Mapping

We interpret Mn^{2+}-induced hyperintensity distant to the injection site at time-points later than the time of injection to be indicative of axonal transport when these sites are connected to the injection site by well-established axonal fiber tracts. For example, Mn^{2+} intensities tracing along the hippocampal fimbria and fornix to the septal nuclei of the basal forebrain, or along the hippocampal commissure to the contralateral hippocampus meets this definition.

A wide range of axonal transport rates for Mn^{2+} (Bearer et al., 2007a), in addition to other tracers, are reported in the literature (Satpute-Krishnan et al., 2006); suggesting a 'leading edge' of Mn^{2+} transport may be present in fiber tracts connected to the injection site. Direct comparisons between time-points (e.g. 7 hours versus 1 hour) do not take into account the potentially confounding effects of such a 'leading edge', should it be below a chosen statistical significance in the direct comparison. Consider a location with a Mn^{2+} induced signal increase at time-point 1. To achieve statistical significance in a direct comparison at time-point 2, a greater Mn^{2+}-induced signal increase is required at this location compared with locations that did not have a Mn^{2+}-induced signal increase at time-point 1. Thus a leading edge of Mn^{2+} transport can undermine direct time-point comparisons.

In the hippocampal injection analysis, we generate three composite time-point comparisons using combinations of direct time-point comparisons. (1) Increase after injection, comparison of 1 hour and pre-injection images (see Supplemental Fig. 1c); (2) Increase at 7 hours, comparison of 7 hours and pre-injection images (see Fig. 3); and (3) Increase at 25 hours, comparison of 25 hours and pre-injection images (see Fig. 4b, 5b). A voxel significant in Comparison (1) can only be significant in Comparison (2) if identified as statistically significant in a direct comparison of 7 hour and 1 hour images. Similarly, voxels significant in Comparison (2) can only be significant in Comparison (3) if identified as statistically significant in a direct comparison of 25 hour and 7 hour images. Images obtained 25 hours after intra-ocular injections were compared to pre-injection images (see Fig. 7). All comparisons were performed in SPM8 using intragroup paired Student's *t*-test and significance was considered reached at $p < 0.00001$, corresponding to a T-value greater than 7.09 ($n = 12$ in all groups).

This analysis method generated maps used to assess inter-group differences by: (1) Visual assessment of the extent of the increases along pathways, at the same time-point; (2) Visual assessment of the time-point at which increases were observed at specific anatomical locations; (3) Numerical assessment of the extent of the increases at specific anatomical locations along a pathway. The segmentation of anatomical structures of interest (e.g. hippocampus, septal nuclei) on the high resolution *in vivo* template used in this study enabled non-biased numerical assessment to take place (see Table 1).

Tensor-based morphometry

A deformation field analysis implemented by Thompson and coworkers (Thompson et al., 2008) was used to analyze whether MRI brain scans of the APP −/− were different from wild type mouse brain scans; processing was implemented in the LONI Pipeline Processing Environment (Rex et al., 2003). Briefly, all pre-injections scans were mapped into a wild type minimum deformation template (MDT) and the resulting displacement field (J^TJ, with J the deformation Jacobian) for each scan determined. An Independent samples *t*-test assessing the difference between the absolute value of the determinants of the displacement fields of the wild type and APP −/− scans identified areas of significant changes in the APP −/− brains. Results are presented in Supplementary Fig. 1b at a significance level of $p < 0.00001$ corresponding to a T-value greater than 7.09 (n = 12). Visualization of the MR images and SPM was performed with Amira (Visage Imaging, San Diego, CA) and MRIcro (Rorden and Brett, 2000).

Results

Injection site location and tissue status are similar in wild type and APP −/− mice

MR images of individual skull-stripped brains and the averaged dataset for all 12 brains for each genotype reveal consistent placement of the injection site in the hippocampus (Fig. 1a). Note that the averaged image preserves anatomical details detected in the image for a single individual, validating alignments and demonstrating the precision of injection location.

Injection sites appear as focal areas of hypointensity within a bright hyperintense halo in MR images taken 1 hour post Mn^{2+} administration (Fig 1a; arrows) due to Mn^{2+} varying effects on relaxation times at different concentrations. The average injection sites were identified as x = −3.2 ± 0.28 mm, y = −4.66 ± 0.42 mm and z = −3.60 ± 0.50 and x = −3.17 ± 0.32 mm, y = −4.76 ± 0.31 mm and z = −3.80 ± 0.43 for wild type and APP −/− mice respectively (n = 12); no significant differences between groups were detected. Injection sites, represented as spheres, overlaid onto coronal, axial and sagittal semi-transparent volumes of the template image illustrate the accuracy of injection placement (Fig 1b; wild type, blue; APP −/−, red).

Our previous work identified minimal glial response following intra-hippocampal Mn^{2+} administration at the volume (5 nl) and concentration (500 mM) used in this study (Bearer et al., 2007b). However, reactive gliosis is a known phenotype of APP −/− mice (Dawson et al., 1999; Zheng et al., 1995); as such it is reasonable to anticipate that APP −/− mice may display an exacerbated inflammatory response following injection. Brain sections prepared from the mice used in this study were assessed for microglial activation (Iba1). No differences between the groups at the injection site were observed (Fig. 1c, d); the injection site appears as a small cavity. Fluorescence microscopy demonstrated rhodamine-dextran fluorescence in an injection site within the hippocampal CA3 subfield of a brain section from an APP −/− mouse (Fig. 1e).

A lower body weight was recorded for APP −/−, compared with wild type, mice (data not shown). Skull-stripped pre-injection images were used to assess the overall brain volume of wild type and APP −/− mice and were consistent with previous reports of this strain of APP −/− mice having reduced brain size (Zheng et al., 1995) (Supplementary Fig. 1a; ** $P < 0.01$; Students *t*-test for independent means). To ensure that areas under investigation in this study were not unduly reduced, tensor-based morphometric (TBM) analysis was performed using the pre-injection images (Supplementary Fig. 1b). The olfactory bulbs, dorsal tenia tecta, thalamus, subiculum and cerebellum were identified as being smaller in APP −/− compared with wild type mice. Importantly, no differences were observed in the hippocampal-forebrain neural circuitry and hippocampal commissures.

Previous neuroanatomical studies of APP −/− strains different from the mice used in this study have reported occurrences of callosal agenesis and hippocampal commissure defects in mice exclusively derived from the 129/SvEv background (Magara et al., 1999). These mice were generated by a 200 kilobase deletion of the APP gene and backcrossed onto either the C57BL/6J or 129/SvEv strain; both showed reductions in brain size. The APP −/− mice used in this study were backcrossed onto the C57BL/6J strain and pre-injection APP −/− images were assessed for corpus callosum presence and no incidences of callosal agenesis or Probst bundle formation were observed (Muller et al., 1994). To assess hippocampal commissure viability, a subset of APP −/− (n = 4) and wild type (n = 2) brains were scanned *ex vivo* overnight using diffusion tensor imaging (DTI). No differences in fractional anisotropy, a measure of tract integrity of the hippocampal commissures, were observed between groups (Supplementary Fig. 1a). Visual assessment of hippocampal commissures in brain sections, prepared from wild type and APP −/− mice, stained for myelin with a modified solochrome technique that accentuates fiber tracks, identified no major commissure defects (after adjusting for brain size) (Supplementary Fig. 2a).

The hyperintense region, encircling the injection site, visible on representative 1 hr images in Fig. 1a indicates passive Mn^{2+} diffusion from the injection site and is commonly found in MEMRI images involving localized intra-cerebral administration (Bearer et al., 2007b; Bearer et al., 2009). Previous studies noting similar patterns record no lack of specificity in subsequently identified projection patterns (Allegrini and Wiessner, 2003; Pautler et al., 2003; Pautler et al., 1998a; Saleem et al., 2002; Van der Linden et al., 2002). The statistically significant signal increases due to Mn^{2+} administration at the 1 hour time-point were assessed by paired Students *t*-test comparisons of the 1 hour and pre-injection skull-stripped and co-registered whole brain images; volumes of 0.93 mm^3 and 0.84 mm^3 were increased in the wild type and APP −/− injection site hippocampi respectively (performed on SPM output calculated to $p < 0.00001$, $T = 7.09$, $n = 12$; Supplementary Fig. 1c, Table 1), demonstrating a consistent reproducible amount of Mn^{2+} had been injected in the two cohorts.

Hippocampal-forebrain axonal transport of Mn^{2+} is reduced in APP −/− mice

Mn^{2+} injected into CA3 of the hippocampus transports along the hippocampal fimbria, down the fornix and arrives in the septal nuclei of the basal forebrain within 6 hours in wild type mice (Bearer et al., 2007b). Segmentation of the hippocampal formation and the septal nuclei illustrate the start- and endpoint structures involved in this transport (Fig. 2a). Coronal MR slices from a representative wildtype mouse, at the 7 hour time-point, demonstrate Mn^{2+}-induced signal intensity at these structures; ipsilateral signal increase in the hippocampal formation (slice positioned at approximately bregma – 3.8 mm) and at the septal nuclei (slice positioned at approximately bregma + 0.4 mm). These signal changes due to axonal transport of Mn^{2+} are observable in axial slices of individual mice from each genotype, and group averages (Fig 2b).

A representative fluorescence micrograph from an APP −/− mouse demonstrates transport of the rhodamine-dextran to the appropriate location, confirming that the injection introduced tracer into the expected circuit originating in the hippocampus (Fig. 2d). No qualitative differences in numbers, size, or location of cholinergic neurons, as detected by ChAT staining, was found in the medial septal nuclei of APP−/− compared to wild type mice (Fig. 2d,e respectively). No significant difference in numbers of Iba1 stained cells, a marker of glial activation, was found between genotypes (Supplementary Materials, Fig. 2b).

Voxelwise SPM of the Mn^{2+}-induced signal increase at 7 hours indicates both groups transport Mn^{2+} along the hippocampal-forebrain pathway (Fig. 3). Overlay of SPM maps

onto slices from the template image enables visual assessment of underlying structures, particularly the dorsal hippocampal commissure, ventral hippocampal commissure and septal nuclei. Significant voxels in the wild type extend further forward and occupy a greater volume of the septal nuclei; 0.39 mm^3 (17% of septal volume) in wild type compared with 0.11 mm^3 (5% of septal volume) in APP−/− (Table 1). Increases detected in the amygdala in wild type at the 7 hour time-point were not observed in APP −/− mice until the 25 hour time-point, and were reduced in volume (Supplemental Fig. 3, Table 1).

Contralateral Mn^{2+} transport is reduced in APP −/− mice

Images taken 25 hours after Mn^{2+} administration demonstrate new signal increases in the contralateral hippocampus, the ipsilateral thalamus, and further anterior along the hippocampal-forebrain circuit in wild type mice (Fig. 4a). Mn^{2+} signal also continues to increase in the septal nuclei. By SPM analysis and comparison to mouse atlases, increases along the hippocampus to forebrain connections extend into the dorsal tenia tecta and nucleus accumbens in both groups, reaching the infralimbic cortex in wild type. Similar to the 7 hour time-point, statistically significant signal appeared further rostral and occupied greater volumes in wild type than in APP −/− mice (Fig. 4b).

Rhodamine-dextran fluorescence appears in the contralateral hippocampus in brain sections prepared from wild type and APP −/− mice (Fig. 5a,b); fluorescence was sharply restricted to the CA2 and CA3 pyramidal layer (white arrowheads) and reduced in APP −/− compared with wild type sections. Visual assessment indicated contralateral Mn^{2+} transport to be greater in wild type, compared with APP −/−, mice (Fig 4b). The increase exclusive to the hippocampal formations are presented within semi-transparent renderings of the hippocampal structure for wildtype and APP −/− groups (Fig. 5c); quantification indicated 24% (3.02 mm^3) of the contralateral hippocampus was increased in wildtype mice, while coverage of only 2% (0.25 mm^3) was observed in APP −/− mice (Fig. 5c, Table 1).

Reduced Mn^{2+} transport in the visual pathway of APP −/− mice

Mn^{2+} enters retinal ganglion cells and travels within their axons in the anterograde direction along the optic nerve to the midbrain where retinal axons terminate in the superior colliculus and lateral geniculate nucleus (Bearer et al., 2007a; Watanabe et al., 2001)(diagrammed in Fig 6a). A coronal MR slice from a representative wild type mouse (approx. −3.8 mm bregma) taken 25 hours after intra-ocular administration, of 0.25 μl of 250 mM Mn^{2+}, illustrates signal enhancement at the superior colliculus (Fig. 6a). At 25 hours after intra-ocular administration, Mn^{2+}-induced signal is visible in the superior colliculus in single images of both wild type and APP−/− individuals, and clear in the averaged images of all 12 animals in both groups (Fig. 6b,c).

SPM analysis reveals intensity increases at the lateral geniculate nucleus and superior colliculus (Fig. 7). In the wild type, Mn^{2+}-induced intensity increases were consistently greater in extent when compared with APP −/−. Quantification of the increases in the lateral geniculate nucleus and superior colliculus identified increases of 0.43 mm^3 (26 % coverage) and 1.81 mm^3 (16 % coverage) in wild type respectively, while in APP −/− mice increases were much less, only 0.28 mm^3 (17 % coverage) and 0.90 mm^3 (6 % coverage) respectively.

Discussion

MEMRI examination of the visual pathway and hippocampal-based circuits, provided the same conclusion: axonal transport is reduced in mice knocked out for the APP gene. We identified reduced Mn^{2+} axonal transport along the fiber tracts from hippocampus to the amygdala and basal forebrain at 7 hours after Mn^{2+} administration, and a reduction in both

rostral and contralateral transport at 25 hours in APP−/− mice. Of special note was a decrease in transport across the midline to the contralateral hippocampus, detected both in the MEMRI image analysis and with co-injected traditional tract tracer, low molecular weight rhodamine-dextran, by histology. This additional detail arises in part from our ability to deliver a small volume of tracer to a precise hippocampal location and also from our large dataset which allowed stringent statistical analysis. In separate experiments a reduction in Mn^{2+} transport in the visual pathway from eye to midbrain and superior colliculus was also observed after intra-ocular administration in APP−/− animals. This result demonstrates a specific role for APP in anterograde transport of Mn^{2+}.

This study supports a critical role for APP in transport, and demonstrates that transport dynamics are witnessed by MEMRI. It is worth noting that the axonal transport reduction detected here occurred in the presence of APP homologues: APLP1 and APLP2 (Heber et al., 2000). These homologues may rescue some of the deficits incurred by the loss of APP, but do not return transport to normal. Similarly, MEMRI identified axonal transport impairments in mice deficient for kinesin-1 light chain (Bearer et al., 2007a) even though there are two other kinesin-1 light chains and several other of the 45 kinesins in the mouse genome are also likely to mediate axonal transport (Hirokawa et al., 2010). Cargo receptors for motors other than the APP family have been reported, such as Jun-interacting proteins (JIP) 1, 2 (Verhey et al., 2001) and JIP 3 (Bowman et al., 2000) and even negatively charged membrane lipids (Klopfenstein et al., 2002). Thus transport is reduced, but not abolished, in mice knocked out for a single component of the redundant and multi-component axonal transport machinery. Whether these multiple components play specialized roles in specific pathways remains unknown. The degree of impairment reported here suggests that APP may be one of the more important components for inter-hippocampal communications not previously recognized. Typically only major differences in transport can be detected using histologic tracers. That we detect a difference here indicates a major defect in inter-hippocampal transport in these APP−/− mice. Such precise mirroring of connections between right and left hippocampal domains has not been previously reported, and is likely due to the precision of placement and the small volume of our injection which labels only a small subset of domain-specific neurons.

MEMRI investigation of axonal transport in hippocampal-based circuitry involves multi-synaptic and bidirectional transport of Mn^{2+}. Although retrograde Mn^{2+} transport has been reported (Matsuda et al., 2010), the speed and extent is unknown with respect to anterograde transport, which appears to dominate Mn^{2+} transport (Pautler et al., 1998b; Sloot and Gramsbergen, 1994; Tjalve et al., 1995). MEMRI work examining axonal transport in the hippocampal-forebrain circuit of a mouse model of Down syndrome identified a marked increase in axonal transport (Bearer et al., 2007b). These mice have a 1.5-fold expression of murine APP. In the APP−/− mice studied here we find the expected diminished transport not only in the hippocampal-forebrain connection but also in hippocampal connections to the amygdala and contralateral hippocampus and in the optic tract. The analogous deficit in the visual-pathway reported here and effects of mutated APP overexpression and APP absence in the olfactory circuit (Minoshima and Cross, 2008; Smith et al., 2010) suggest axonal transport dependence on APP is not regional. Our work extends previous studies, confirming that APP is involved in modulating axonal transport in a main learning and memory circuit. Furthermore, APP overexpression disrupts hippocampal-based retrograde transport of nerve growth factor (NGF) to basal forebrain cholinergic neurons, leading to neuron degeneration (Salehi et al., 2006) suggesting APP manipulation can lead to bi-directional transport deficits.

Previous studies have identified an age-related reduction in axonal transport in the olfactory bulbs of rats and mice (Cross et al., 2008; Smith et al., 2010). Through utilization of the

methodology presented in this study, we would expect to identify analogous axonal transport deficits in hippocampal-based circuitry and the optic tract. However, in animal models involving genetic manipulation of APP, it is reasonable to suggest APP-mediated alterations to axonal transport would predominate alterations due to age. As such, examination at a single age-point appears sufficient in consideration of APP-mediated changes to axonal transport but studies examining the efficacy of pharmacological interventions may benefit from consideration of the age-related changes (Smith et al., 2011). We chose to study mice younger than 6 months old as non-specific reactive gliosis has been reported in older animals (Zheng et al., 1995).

In addition to the axonal transport deficits due to APP loss, alterations in trans-synaptic trafficking of Mn^{2+} and cellular electrophysiology may also modulate Mn^{2+} presence distal to the injection site. Pre-synaptic reduction of APP and APLP2 (via siRNA) decreased synaptic efficacy *in vivo* (Herard et al., 2006). While the concomitant reduction in APLP2 makes extension to APP deficient mice complex, it is reasonable to suggest that a reduction in synaptic efficacy may also contribute to the findings in this study. Electrical activity is not required for Mn^{2+} uptake but it is necessary for trans-synaptic transport of Mn^{2+} (Bearer et al., 2007a). Electrophysiological assessment of APP −/− mice reported an impairment in hippocampal LTP at 8 – 12 months of age, in addition to identifying a disruption in the pre-synaptic marker synaptophysin (Dawson et al., 1999; Seabrook et al., 1999). However, the mice used here are significantly younger and there are no reports of LTP impairment or reductions in synaptic markers for young APP −/− mice. Thus the main effect of APP loss, with respect to Mn^{2+} transport, in this cohort would be transport dysfunction.

Our results may also point to a biochemical cellular basis for behavioural defects described in the APP−/− mouse. Pathway-specific alterations due to APP loss may affect Mn^{2+} transport because of underlying connectivity strength differences; MEMRI studies have provided evidence that the level of functional connectivity between two separate anatomical regions can influence the extent of axonal transport of Mn^{2+} (Michaelis et al., 2004; Van der Linden et al., 2002; van der Zijden et al., 2007). Deficits in passive avoidance (Senechal et al., 2008) and conditioned avoidance learning paradigms (Dawson et al., 1999) in APP −/− mice at 10 months of age have been reported; these tasks are thought to involve the hippocampus and amygdala. Indeed, we identify a reduction in axonal transport in hippocampal-amygdala connections in APP −/− mice at 3 – 4 months of age.

APP plays an important role in memory (Dodart et al., 2000) and APP deletion, overexpression and mutation have been found to lead to impairments in a variety of learning paradigms (Granholm et al., 2003; Puolivali et al., 2002). Through its capacity to influence axonal transport - either by absence, mutation or overexpression - APP could impair the brain via failures in the delivery of a potentially wide range of molecules necessary for learning and memory. If a correlation to Alzheimer's disease were to be made, where the toxic fragment of APP, Aβ, induces axonal transport impairments, these impairments are unlikely to resemble single unit deficits, such as those produced by APP loss reported here (Stokin et al., 2005). It may be that Aβ-deposition disrupts transport in more complex ways than the absence of a single unit of the axonal transport machinery.

Previous MEMRI work reported a deficit of Mn^{2+} transport in the olfactory bulbs, after nasal delivery, in APP−/− mice (Smith et al., 2010). The primary advance in the work presented here is a demonstration, via both MEMRI and classical tracer methods, that APP is required for movement of Mn^{2+} along well established axonal fiber bundles in specific neuronal circuits. Our study reveals a dependence on APP for transport along these bundles in the key memory circuit from hippocampal to septal nuclei and basal forebrain. The extension of this finding to the visual pathway and rigorous assessment of putative

morphological changes in the circuits examined strengthen the key conclusion that APP is a key component of transport in the central nervous system. Our studies indicate MEMRI imaging will provide insight into the effects of Aβ on transport dynamics in subsequent studies.

Summary

Here we demonstrate APP is required for normal axonal transport in hippocampal-based circuitry prone to plaque deposition and implicated in many of the higher level executive functions that undergo degeneration in AD. Replication of this finding in the visual pathway also reported here confirms the system-wide involvement of APP in axonal transport.

Supplementary Material

Refer to Web version on PubMed Central for supplementary material.

Acknowledgments

We would like to acknowledge the contributions of Dr. Benoit Boulat for help with MR imaging and Grace Cai for help with image pre-processing; Kathleen Kilpatrick for lab management and coordination of projects; Aaron Gonzales and Anna Vestling for digital image analysis support in the Bearer lab; and Drs. Art Toga and Ivo Dinov and graduate student Alen Zamanyan at the Laboratory for NeuroImaging at UCLA for invaluable assistance with LONI pipeline and TBM analysis. This project was funded in part by NINDS NS062184 (ELB) and the Beckman Institute (REJ).

Abbreviations

AD	Alzheimer's disease
APP	Amyloid precursor protein
APLP1	Amyloid precursor-like protein 1
APLP2	Amyloid precursor-like protein 2
Aβ	amyloid-β
ChAT	choline acetyltransferase
Iba1	Ionized calcium binding adaptor molecule 1
NGF	nerve growth factor
NFT	Neurofibrillary tangles
MEMRI	Manganese-enhanced MRI
SPM	Statistical parametric mapping
TBM	tensor-based morphometry

References

Allegrini PR, Wiessner C. Three-dimensional MRI of cerebral projections in rat brain in vivo after intracortical injection of MnCl2. Nmr in Biomedicine. 2003; 16:252–256. [PubMed: 14648884]

Aoki I, Wu YJL, Silva AC, Lynch RM, Koretsky AP. In vivo detection of neuroarchitecture in the rodent brain using manganese-enhanced MRI. Neuroimage. 2004; 22:1046–1059. [PubMed: 15219577]

Bearer EL, Falzone TL, Zhang X, Biris O, Rasin A, Jacobs RE. Role of neuronal activity and kinesin on tract tracing by manganese-enhanced MRI (MEMRI). Neuroimage. 2007a; 37(Suppl 1):S37–S46. [PubMed: 17600729]

Bearer EL, Zhang X, Jacobs RE. Live imaging of neuronal connections by magnetic resonance: Robust transport in the hippocampal-septal memory circuit in a mouse model of Down syndrome. Neuroimage. 2007b; 37:230–242. [PubMed: 17566763]

Bearer EL, Zhang X, Janvelyan D, Boulat B, Jacobs RE. Reward circuitry is perturbed in the absence of the serotonin transporter. Neuroimage. 2009; 46:1091–1104. [PubMed: 19306930]

Biomedical Research and Services Section, N.I.H. Medical Image Processing, Analysis and Visualization (MIPAV). 2011

Bowman AB, Kamal A, Ritchings BW, Philp AV, McGrail M, Gindhart JG, Goldstein LS. Kinesin-dependent axonal transport is mediated by the sunday driver (SYD) protein. Cell. 2000; 103:583–594. [PubMed: 11106729]

Cross DJ, Flexman JA, Anzai Y, Maravilla KR, Minoshima S. Age-related decrease in axonal transport measured by MR imaging in vivo. Neuroimage. 2008; 39:915–926. [PubMed: 17980625]

Dawson GR, Seabrook GR, Zheng H, Smith DW, Graham S, O'Dowd G, Bowery BJ, Boyce S, Trumbauer ME, Chen HY, Van der Ploeg LHT, Sirinathsinghji DJS. Age-related cognitive deficits, impaired long-term potentiation and reduction in synaptic marker density in mice lacking the beta-amyloid precursor protein. Neuroscience. 1999; 90:1–13. [PubMed: 10188929]

Dodart JC, Mathis C, Ungerer A. The beta-amyloid precursor protein and its derivatives: from biology to learning and memory processes. Rev Neurosci. 2000; 11:75–93. [PubMed: 10718147]

Granholm ACE, Hunter CL, Bimonte HA. Behavioral comparison of 4 and 6 month-old Ts65Dn mice: Age-related impairments in working and reference memory. Behavioural Brain Research. 2003; 138:121–131. [PubMed: 12527443]

Gunawardena S, Goldstein LS. Disruption of axonal transport and neuronal viability by amyloid precursor protein mutations in Drosophila. Neuron. 2001; 32:389–401. [PubMed: 11709151]

Hasan KM, Basser PJ, Parker DL, Alexander AL. Analytical computation of the eigenvalues and eigenvectors in DT-MRI. Journal of Magnetic Resonance. 2001; 152:41–47. [PubMed: 11531362]

Heber S, Herms J, Gajic V, Hainfellner J, Aguzzi A, Rulicke T, von Kretzschmar H, von Koch C, Sisodia S, Tremml P, Lipp HP, Wolfer DP, Muller U. Mice with combined gene knockouts reveal essential and partially redundant functions of amyloid precursor protein family members. J Neurosci. 2000; 20:7951–7963. [PubMed: 11050115]

Hennig J, Nauerth A, Friedburg H. RARE imaging: a fast imaging method for clinical MR. Magn Reson Med. 1986; 3:823–833. [PubMed: 3821461]

Herard AS, Besret L, Dubois A, Dauguet J, Delzescaux T, Hantraye P, Bonvento G, Moya KL. siRNA targeted against amyloid precursor protein impairs synaptic activity in vivo. Neurobiol Aging. 2006; 27:1740–1750. [PubMed: 16337035]

Herms J, Anliker B, Heber S, Ring S, Fuhrmann M, Kretzschmar H, Sisodia S, Muller U. Cortical dysplasia resembling human type 2 lissencephaly in mice lacking all three APP family members. EMBO J. 2004; 23:4106–4115. [PubMed: 15385965]

Hirokawa N, Niwa S, Tanaka Y. Molecular motors in neurons: transport mechanisms and roles in brain function, development, and disease. Neuron. 2010; 68:610–638. [PubMed: 21092854]

Ishihara T, Gondo T, Takahashi M, Uchino F, Ikeda S, Allsop D, Imai K. Immunohistochemical and immunoelectron microscopical characterization of cerebrovascular and senile plaque amyloid in aged dogs' brains. Brain Res. 1991; 548:196–205. [PubMed: 1868335]

Kamal A, Almenar-Queralt A, LeBlanc JF, Roberts EA, Goldstein LS. Kinesin-mediated axonal transport of a membrane compartment containing beta-secretase and presenilin-1 requires APP. Nature. 2001; 414:643–648. [PubMed: 11740561]

Kamal A, Stokin GB, Yang Z, Xia CH, Goldstein LS. Axonal transport of amyloid precursor protein is mediated by direct binding to the kinesin light chain subunit of kinesin-I. Neuron. 2000; 28:449–459. [PubMed: 11144355]

Keller JN. Age-related neuropathology, cognitive decline, and Alzheimer's disease. Ageing Res Rev. 2006; 5:1–13. [PubMed: 16084778]

Kim J, Choi IY, Michaelis ML, Lee P. Quantitative in vivo measurement of early axonal transport deficits in a triple transgenic mouse model of Alzheimer's disease using manganese-enhanced MRI. Neuroimage. 2011; 56:1286–1292. [PubMed: 21338698]

Klopfenstein DR, Tomishige M, Stuurman N, Vale RD. Role of phosphatidylinositol(4,5)bisphosphate organization in membrane transport by the Unc104 kinesin motor. Cell. 2002; 109:347–358. [PubMed: 12015984]

Lazarov O, Morfini GA, Lee EB, Farah MH, Szodorai A, DeBoer SR, Koliatsos VE, Kins S, Lee VM, Wong PC, Price DL, Brady ST, Sisodia SS. Axonal transport, amyloid precursor protein, kinesin-1, and the processing apparatus: revisited. J Neurosci. 2005; 25:2386–2395. [PubMed: 15745965]

Lin YJ, Koretsky AP. Manganese ion enhances T1-weighted MRI during brain activation: an approach to direct imaging of brain function. Magn Reson Med. 1997; 38:378–388. [PubMed: 9339438]

Magara F, Muller U, Li ZW, Lipp HP, Weissmann C, Stagljar M, Wolfer DP. Genetic background changes the pattern of forebrain commissure defects in transgenic mice underexpressing the beta-amyloid-precursor protein. Proceedings of the National Academy of Sciences of the United States of America. 1999; 96:4656–4661. [PubMed: 10200318]

Matsuda K, Wang HX, Suo C, McCombe D, Horne MK, Morrison WA, Egan GF. Retrograde axonal tracing using manganese enhanced magnetic resonance imaging. Neuroimage. 2010; 50:366–374. [PubMed: 20074651]

Merritt JE, Jacob R, Hallam TJ. Use of manganese to discriminate between calcium influx and mobilization from internal stores in stimulated human neutrophils. J Biol Chem. 1989; 264:1522–1527. [PubMed: 2536366]

Michaelis T, Watanabe T, Frahm J. Functional mapping of neural pathways in rodent brain in vivo using manganese-enhanced three-dimensional magnetic resonance imaging. Nmr in Biomedicine. 2004; 17:554–568. [PubMed: 15617054]

Minoshima S, Cross D. In vivo imaging of axonal transport using MRI: aging and Alzheimer's disease. Eur J Nucl Med Mol Imaging. 2008; 35(Suppl 1):S89–S92. [PubMed: 18204931]

Muller U, Cristina N, Li ZW, Wolfer DP, Lipp HP, Rulicke T, Brandner S, Aguzzi A, Weissmann C. Behavioral and Anatomical Deficits in Mice Homozygous for a Modified Beta-Amyloid Precursor Protein Gene. Cell. 1994; 79:755–765. [PubMed: 8001115]

Muresan V, Varvel NH, Lamb BT, Muresan Z. The cleavage products of amyloid-beta precursor protein are sorted to distinct carrier vesicles that are independently transported within neurites. J Neurosci. 2009; 29:3565–3578. [PubMed: 19295161]

Pautler RG. In vivo, trans-synaptic tract-tracing utilizing manganese-enhanced magnetic resonance imaging (MEMRI). Nmr in Biomedicine. 2004; 17:595–601. [PubMed: 15761948]

Pautler RG, Mongeau R, Jacobs RE. In vivo trans-synaptic tract tracing from the murine striatum and amygdala utilizing manganese enhanced MRI (MEMRI). Magnetic Resonance in Medicine. 2003; 50:33–39. [PubMed: 12815676]

Pautler RG, Silva AC, Koretsky AP. In vivo neuronal tract tracing using manganese-enhanced magnetic resonance imaging. Magnetic Resonance in Medicine. 1998a; 40:740–748. [PubMed: 9797158]

Paxinos G, Franklin K. The Mouse Brain in Stereotaxix Coordinates. 2001

Price DL, Wong PC, Markowska AL, Lee MK, Thinakaren G, Cleveland DW, Sisodia SS, Borchelt DR. The value of transgenic models for the study of neurodegenerative diseases. Ann N Y Acad Sci. 2000; 920:179–191. [PubMed: 11193148]

Puolivali J, Wang J, Heikkinen T, Heikkila M, Tapiola T, van Groen T, Tanila H. Hippocampal A beta 42 levels correlate with spatial memory deficit in APP and PS1 double transgenic mice. Neurobiology of Disease. 2002; 9:339–347. [PubMed: 11950278]

Rex DE, Ma JQ, Toga AW. The LONI Pipeline Processing Environment. Neuroimage. 2003; 19:1033–1048. [PubMed: 12880830]

Rorden C, Brett M. Stereotaxic display of brain lesions. Behav Neurol. 2000; 12:191–200. [PubMed: 11568431]

Saleem KS, Pauls JM, Augath M, Trinath T, Prause BA, Hashikawa T, Logothetis NK. Magnetic resonance imaging of neuronal connections in the macaque monkey. Neuron. 2002; 34:685–700. [PubMed: 12062017]

Salehi A, Delcroix JD, Belichenko PV, Zhan K, Wu C, Valletta JS, Takimoto-Kimura R, Kleschevnikov AM, Sambamurti K, Chung PP, Xia W, Villar A, Campbell WA, Kulnane LS,

Nixon RA, Lamb BT, Epstein CJ, Stokin GB, Goldstein LS, Mobley WC. Increased App expression in a mouse model of Down's syndrome disrupts NGF transport and causes cholinergic neuron degeneration. Neuron. 2006; 51:29–42. [PubMed: 16815330]

Satpute-Krishnan P, DeGiorgis JA, Conley MP, Jang M, Bearer EL. A peptide zipcode sufficient for anterograde transport within amyloid precursor protein. Proc Natl Acad Sci U S A. 2006; 103:16532–16537. [PubMed: 17062754]

Seabrook GR, Smith DW, Bowery BJ, Easter A, Reynolds T, Fitzjohn SM, Morton RA, Zheng H, Dawson GR, Sirinathsinghji DJ, Davies CH, Collingridge GL, Hill RG. Mechanisms contributing to the deficits in hippocampal synaptic plasticity in mice lacking amyloid precursor protein. Neuropharmacology. 1999; 38:349–359. [PubMed: 10219973]

Senechal Y, Kelly PH, Dev KK. Amyloid precursor protein knockout mice show age-dependent deficits in passive avoidance learning. Behavioural Brain Research. 2008; 186:126–132. [PubMed: 17884188]

Shah SB, Nolan R, Davis E, Stokin GB, Niesman I, Canto I, Glabe C, Goldstein LS. Examination of potential mechanisms of amyloid-induced defects in neuronal transport. Neurobiology of Disease. 2009; 36:11–25. [PubMed: 19497367]

Shattuck DW, Leahy RM. Automated graph-based analysis and correction of cortical volume topology. IEEE Trans Med Imaging. 2001; 20:1167–1177. [PubMed: 11700742]

Silva AC, Lee JH, Aoki I, Koretsky AP. Manganese-enhanced magnetic resonance imaging (MEMRI): methodological and practical considerations. Nmr in Biomedicine. 2004; 17:532–543. [PubMed: 15617052]

Sloot WN, Gramsbergen JB. Axonal transport of manganese and its relevance to selective neurotoxicity in the rat basal ganglia. Brain Res. 1994; 657:124–132. [PubMed: 7820609]

Smith KD, Kallhoff V, Zheng H, Pautler RG. In vivo axonal transport rates decrease in a mouse model of Alzheimer's disease. Neuroimage. 2007; 35:1401–1408. [PubMed: 17369054]

Smith KD, Paylor R, Pautler RG. R-flurbiprofen improves axonal transport in the Tg2576 mouse model of Alzheimer's disease as determined by MEMRI. Magn Reson Med. 2011; 65:1423–1429. [PubMed: 21500269]

Smith KD, Peethumnongsin E, Lin H, Zheng H, Pautler RG. Increased Human Wildtype Tau Attenuates Axonal Transport Deficits Caused by Loss of APP in Mouse Models. Magn Reson Insights. 2010; 4:11–18. [PubMed: 20798780]

Stokin GB, Lillo C, Falzone TL, Brusch RG, Rockenstein E, Mount SL, Raman R, Davies P, Masliah E, Williams DS, Goldstein LS. Axonopathy and transport deficits early in the pathogenesis of Alzheimer's disease. Science. 2005; 307:1282–1288. [PubMed: 15731448]

Thompson PM, Hua X, Leow AD, Lee S, Klunder AD, Toga AW, Lepore N, Chou YY, Brun C, Chiang MC, Barysheva M, Jack CR, Bernstein MA, Britson PJ, Ward CP, Whitwell JL, Borowski B, Fleisher AS, Fox NC, Boyes RG, Barnes J, Harvey D, Kornak J, Schuff N, Boreta L, Alexander GE, Weiner MW, Initi AsDN. 3D characterization of brain atrophy in Alzheimer's disease and mild cognitive impairment using tensor-based morphometry. Neuroimage. 2008; 41:19–34. [PubMed: 18378167]

Tjalve H, Mejare C, Borg-Neczak K. Uptake and transport of manganese in primary and secondary olfactory neurones in pike. Pharmacol Toxicol. 1995; 77:23–31. [PubMed: 8532608]

Torroja L, Chu H, Kotovsky I, White K. Neuronal overexpression of APPL, the Drosophila homologue of the amyloid precursor protein (APP), disrupts axonal transport. Curr Biol. 1999; 9:489–492. [PubMed: 10322116]

Van der Linden A, Verhoye M, Van Meir V, Tindemans I, Eens M, Absil P, Balthazart J. In vivo manganese-enhanced magnetic resonance imaging reveals connections and functional properties of the songbird vocal control system. Neuroscience. 2002; 112:467–474. [PubMed: 12044464]

van der Zijden JP, Wu O, van der Toorn A, Roeling TP, Bleys RLAW, Dijkhuizen RM. Changes in neuronal connectivity after stroke in rats as studied by serial manganese-enhanced MRI. Neuroimage. 2007; 34:1650–1657. [PubMed: 17175175]

Verhey KJ, Meyer D, Deehan R, Blenis J, Schnapp BJ, Rapoport TA, Margolis B. Cargo of kinesin identified as JIP scaffolding proteins and associated signaling molecules. J Cell Biol. 2001; 152:959–970. [PubMed: 11238452]

Walsh DM, Selkoe DJ. A beta oligomers - a decade of discovery. J Neurochem. 2007; 101:1172–1184. [PubMed: 17286590]

Watanabe T, Michaelis T, Frahm J. Mapping of retinal projections in the living rat using high-resolution 3D gradient-echo MRI with Mn2+-induced contrast. Magnetic Resonance in Medicine. 2001; 46:424–429. [PubMed: 11550231]

Wirths O, Weis J, Szczygielski J, Multhaup G, Bayer TA. Axonopathy in an APP/PS1 transgenic mouse model of Alzheimer's disease. Acta Neuropathol. 2006; 111:312–319. [PubMed: 16520967]

Young-Pearse TL, Bai J, Chang R, Zheng JB, LoTurco JJ, Selkoe DJ. A critical function for beta-amyloid precursor protein in neuronal migration revealed by in utero RNA interference. J Neurosci. 2007; 27:14459–14469. [PubMed: 18160654]

Zhang X, Bearer EL, Boulat B, Hall FS, Uhl GR, Jacobs RE. Altered neurocircuitry in the dopamine transporter knockout mouse brain. PLoS One. 2010; 5:e11506. [PubMed: 20634895]

Zheng H, Jiang MH, Trumbauer ME, Sirinathsinghji DJS, Hopkins R, Smith DW, Heavens RP, Dawson GR, Boyce S, Conner MW, Stevens KA, Slunt HH, Sisodia SS, Chen HY, Vanderploeg LHT. Beta-Amyloid Precursor Protein-Deficient Mice Show Reactive Gliosis and Decreased Locomotor-Activity. Cell. 1995; 81:525–531. [PubMed: 7758106]

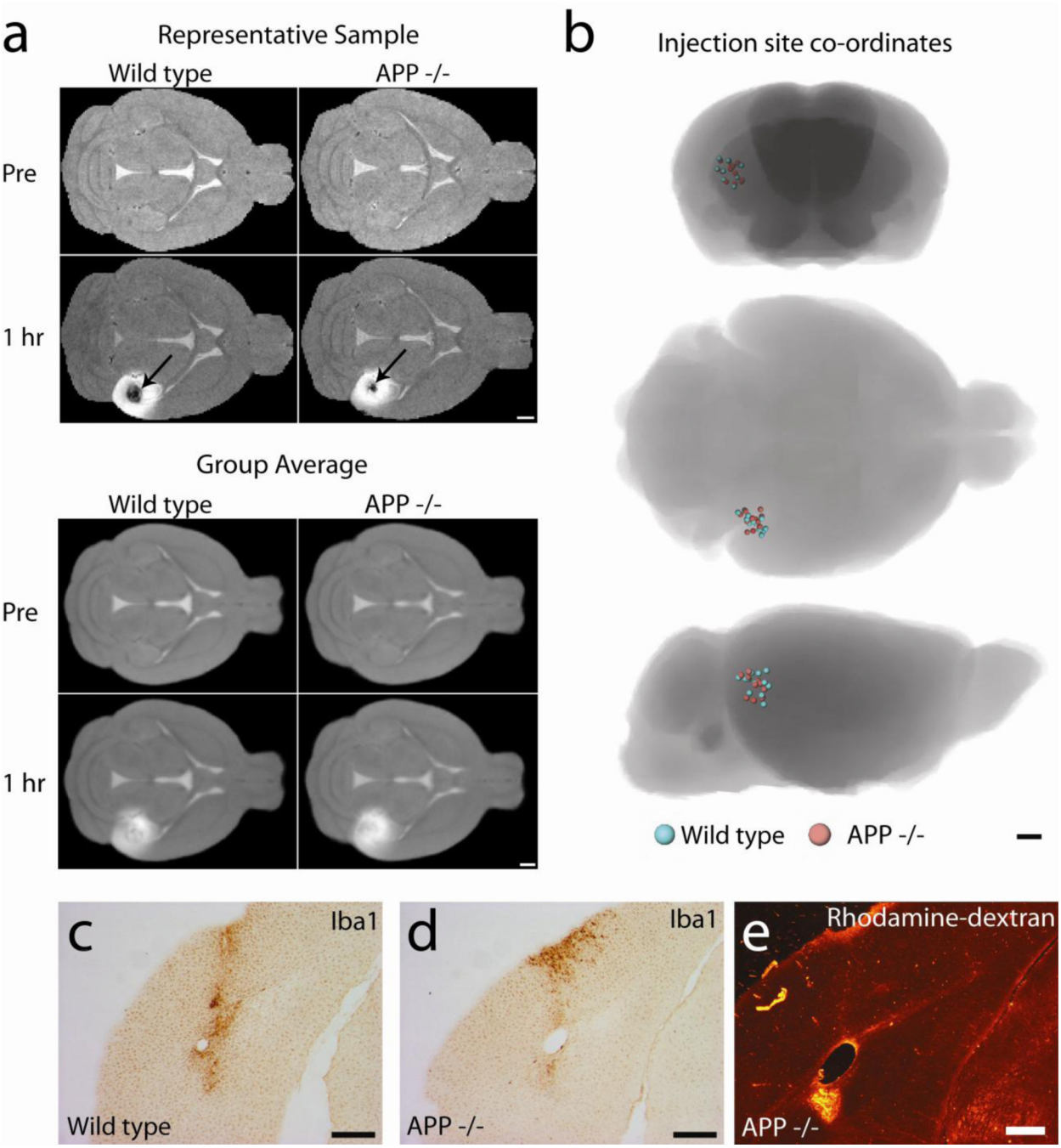

Figure 1. Injection site location and tissue status are similar in wild type and APP −/− mice

(a) Representative and group average MR axial images before (Pre) and 1 hour (1 hr) after intra-hippocampal Mn^{2+} administration are presented (scale bar = 1 mm). Visual inspection of the Mn^{2+} signal enhancement identifies an initially focal pattern after 1 hour (the area of hypointensity is used to generate injection site co-ordinates; denoted by an arrow). (b) Injection site locations, represented as a sphere for each animal used in the statistical analysis of hippocampal injections, confirms placement in the hippocampal CA3 subfield for both groups (blue and red spheres correspond to wild type and APP −/− mice respectively). Injection sites locations have been overlaid onto coronal, axial and saggital semi-transparent rendered images of the MRI template (Scale bar = 1 mm). (c) and (d)

Representative micrographs of Iba1 staining to assess microglial activation at the injection site from wild type and APP −/− mice are presented (Magnification x20; Scale bar = 200 μm). (e) A representative fluorescent micrograph identifying the injection site in a brain section prepared from an APP −/− mouse co-injected with Mn^{2+} and rhodamine-dextran is also presented (magnification x40 and scale bar = 200 μm).

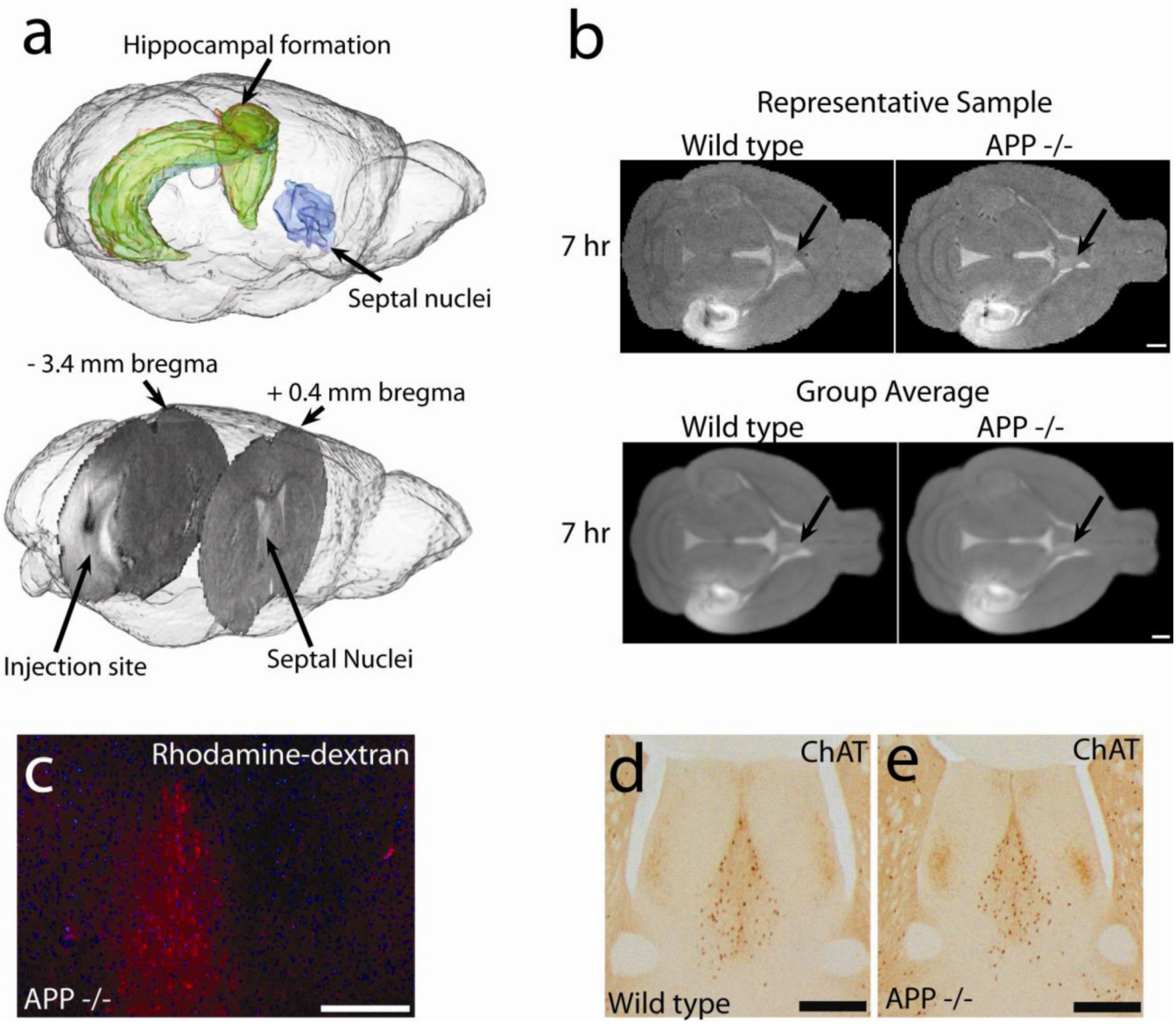

Figure 2. Hippocampal to forebrain axonal transport of Mn^{2+} is detectable at 7 hours post-injection

(b) To aid visualization of Mn^{2+} transport following hippocampal injection a rendering of the template brain surface with the hippocampus (green) and septal nuclei (blue) structures identified is presented. Coronal MR slices from a representative wild type mouse, obtained 7 hours following injection, at the injection site (approx. −3.4 mm bregma) and in the forebrain, at the position of the septal nuclei (approx. +0.4 mm bregma), demonstrate signal increases due to Mn^{2+} transport from the injection site. (b) Representative and group average MR axial images 7 hours following intra-hippocampal Mn^{2+} administration (scale bar = 1 mm) are presented; visual assessment identifies a diffuse pattern of signal enhancement within the injected hippocampus and an increase at the septal nuclei. (c) A representative fluorescent micrographs of brain sections prepared from a representative APP −/− mouse co-injected with Mn^{2+} and rhodamine-dextran demonstrate an increase in fluorescence at the septal nuclei (magnification x40, scale bar = 200 μm). (d) and (e) Representative micrographs of ChAT-stained brain sections, prepared from wild type and

APP −/− mice, at the level of the septal nuclei, are presented (magnification x20; scale bar = 0.5 mm).

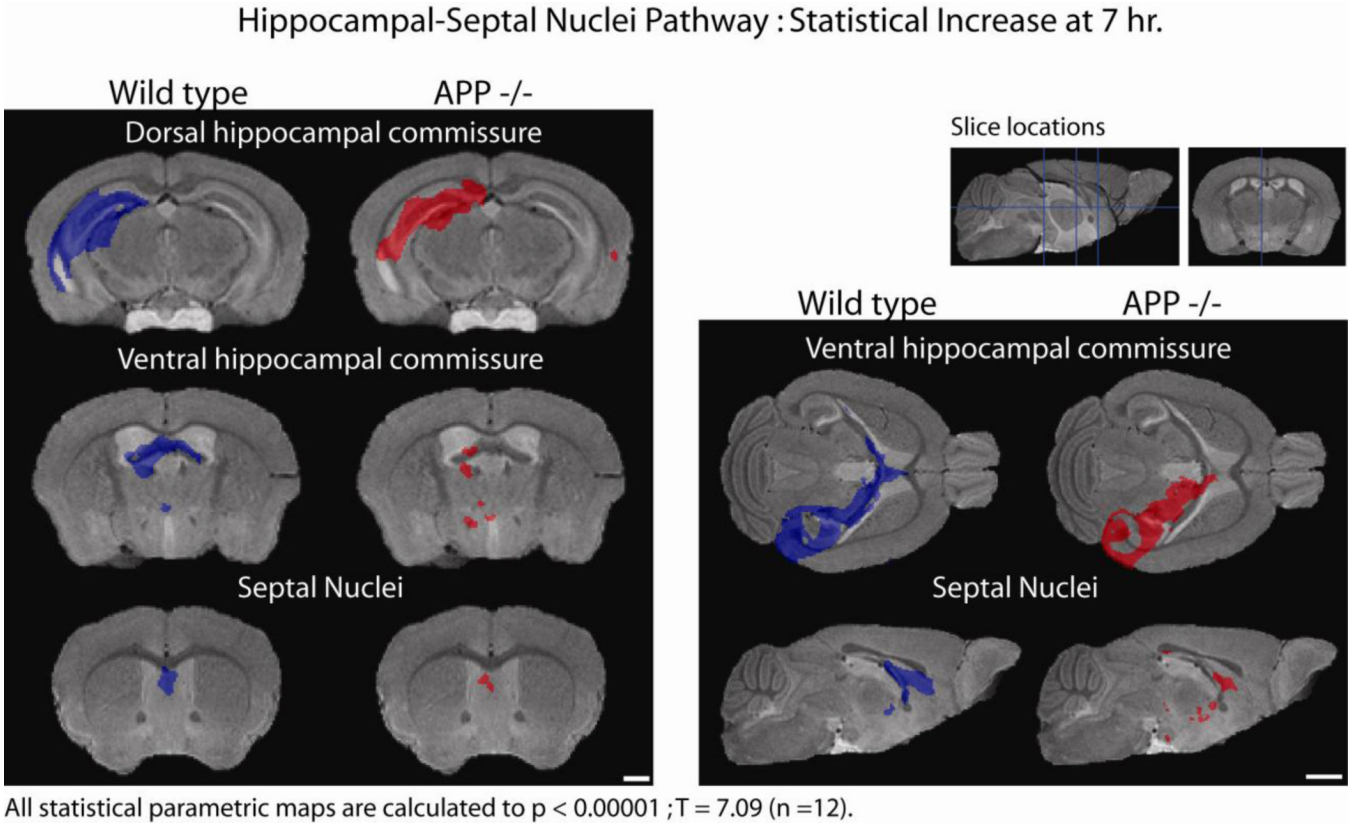

Figure 3. Hippocampal to forebrain axonal transport of Mn^{2+} is reduced in APP −/− mice

Statistical parametric analysis illustrating the increase in signal enhancement due to Mn^{2+} transport at 7 hours in wild type (blue) and APP −/− (red) mice are presented. The statistical parametric maps indicate changes at the dorsal hippocampal commissure (bregma −2.30 mm), ventral hippocampal commissure (−0.46 mm from midline) and the septal nuclei (bregma +0.98 mm, +0.24 mm from midline). All statistical parametric maps are calculated to $p < 0.00001$ ($T = 7.09$; $n = 12$).

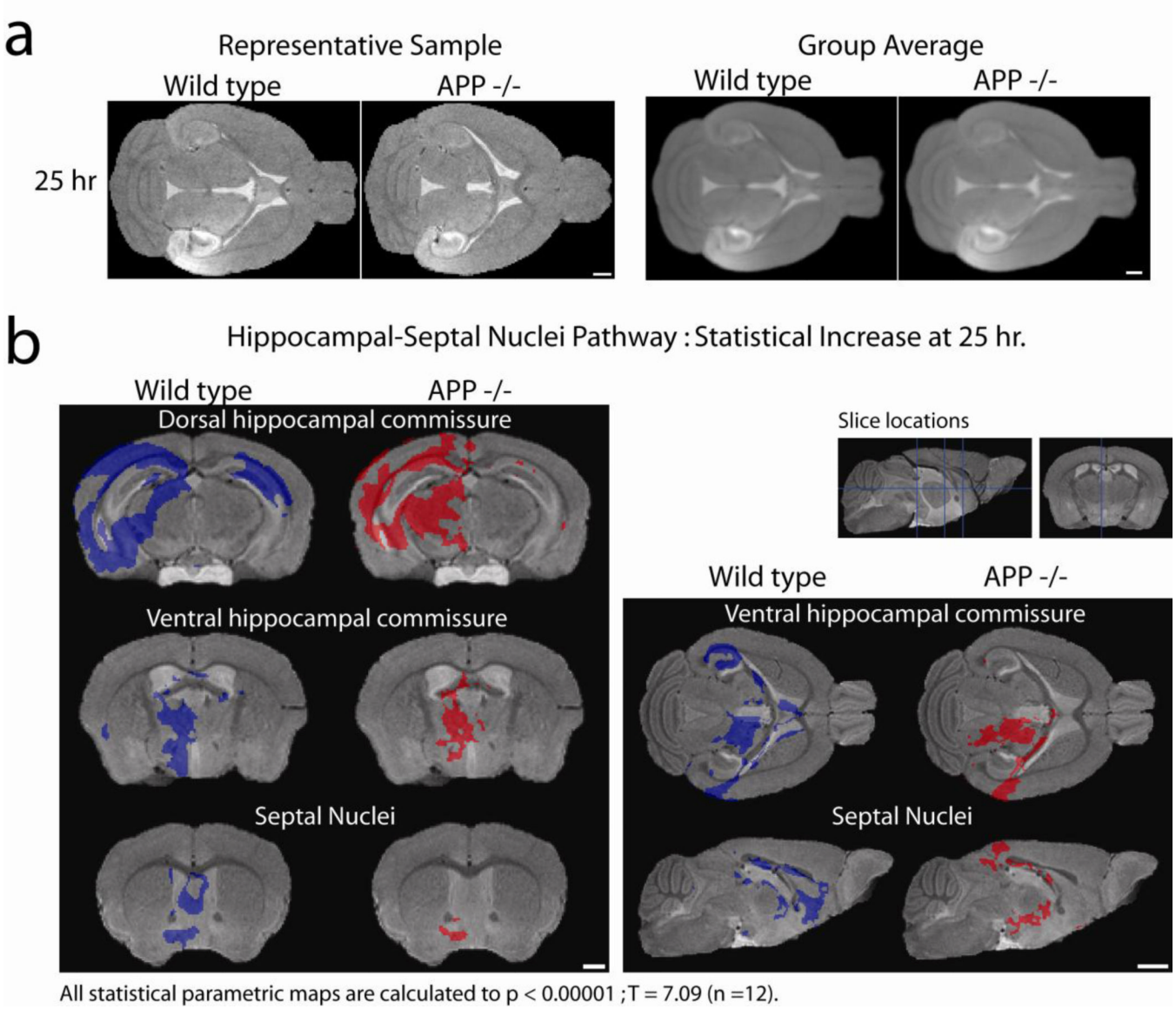

Figure 4. Contralateral Mn^{2+} transport is reduced in APP −/− mice at 25 hr post injection

(a) Representative and group average MR axial images 25 hours following intra-hippocampal Mn^{2+} administration (scale bar = 1 mm); visual assessment identifies continuing signal increase in the septal nuclei and an increase in the contralateral hippocampus. (b) Statistical parametric maps illustrating the increase in signal enhancement due to Mn^{2+} transport at 25 hours in wild type (blue) and APP −/− (red) mice are presented. The statistical parametric maps indicate changes at the dorsal hippocampal commissure (bregma −2.30 mm), ventral hippocampal commissure (bregma −0.46 mm) and the septal nuclei (bregma +0.98 mm, +0.24 mm from midline). All statistical parametric maps are calculated to $p < 0.00001$ ($T = 7.09$; $n = 12$).

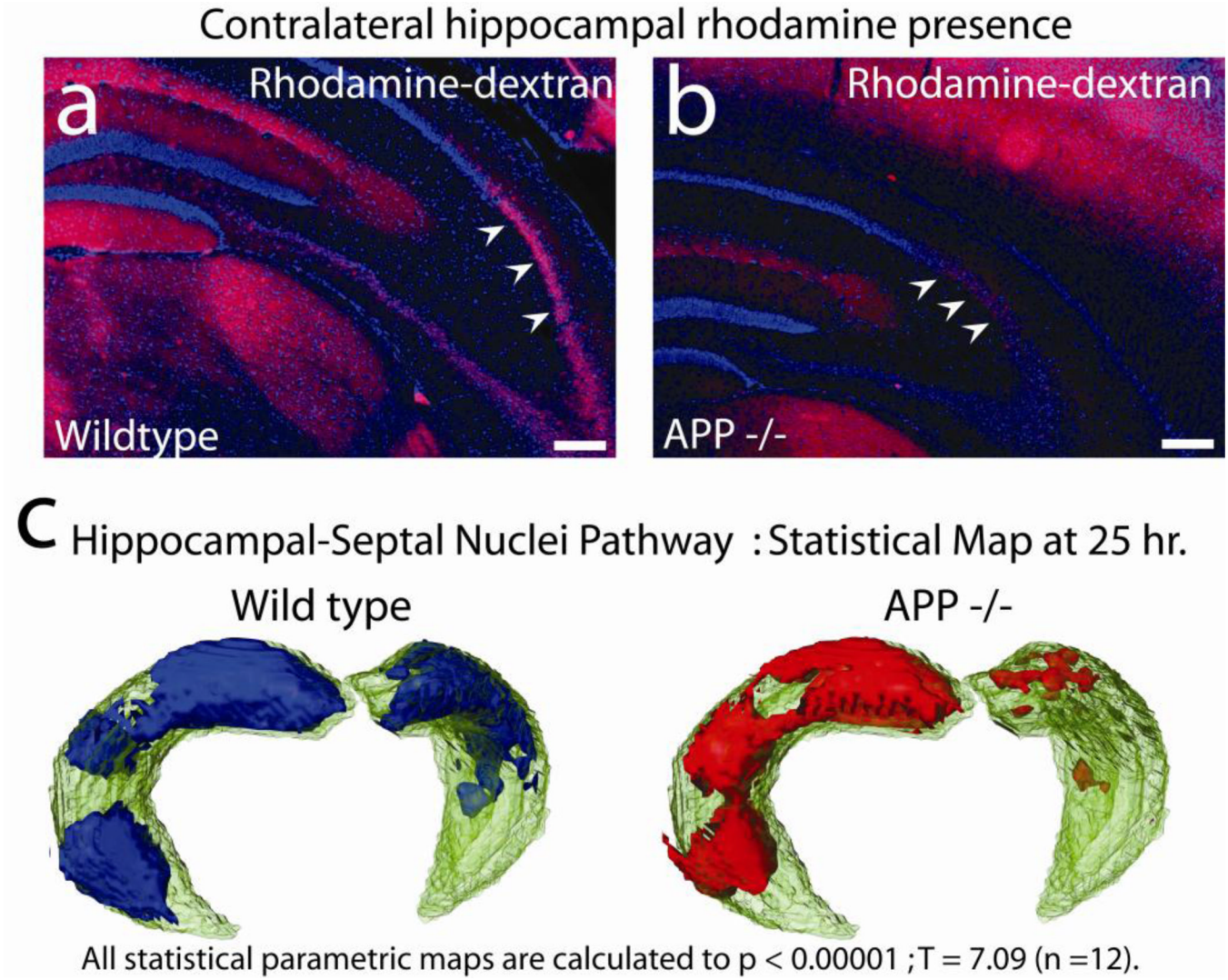

Figure 5. Contralateral Mn^{2+} and rhodamine-dextran transport to the contralateral hippocampus is reduced in APP −/− mice

(a) and (b), representative fluorescent micrographs of brain sections prepared from wild type and APP −/− mice co-injected with Mn^{2+} and rhodamine-dextran identify greater levels of rhodamine-dextran present in the contralateral hippocampus (denoted by white arrowheads) of wild type compared with APP −/− mice (magnification x40, scale bar = 200 μm). (c) The statistical parametric increases exclusive to the hippocampus formation are presented within semi-transparent renderings of the hippocampal structure for wild type and APP −/− mice. All statistical parametric maps are calculated to $p < 0.00001$ ($T = 7.09$; $n = 12$).

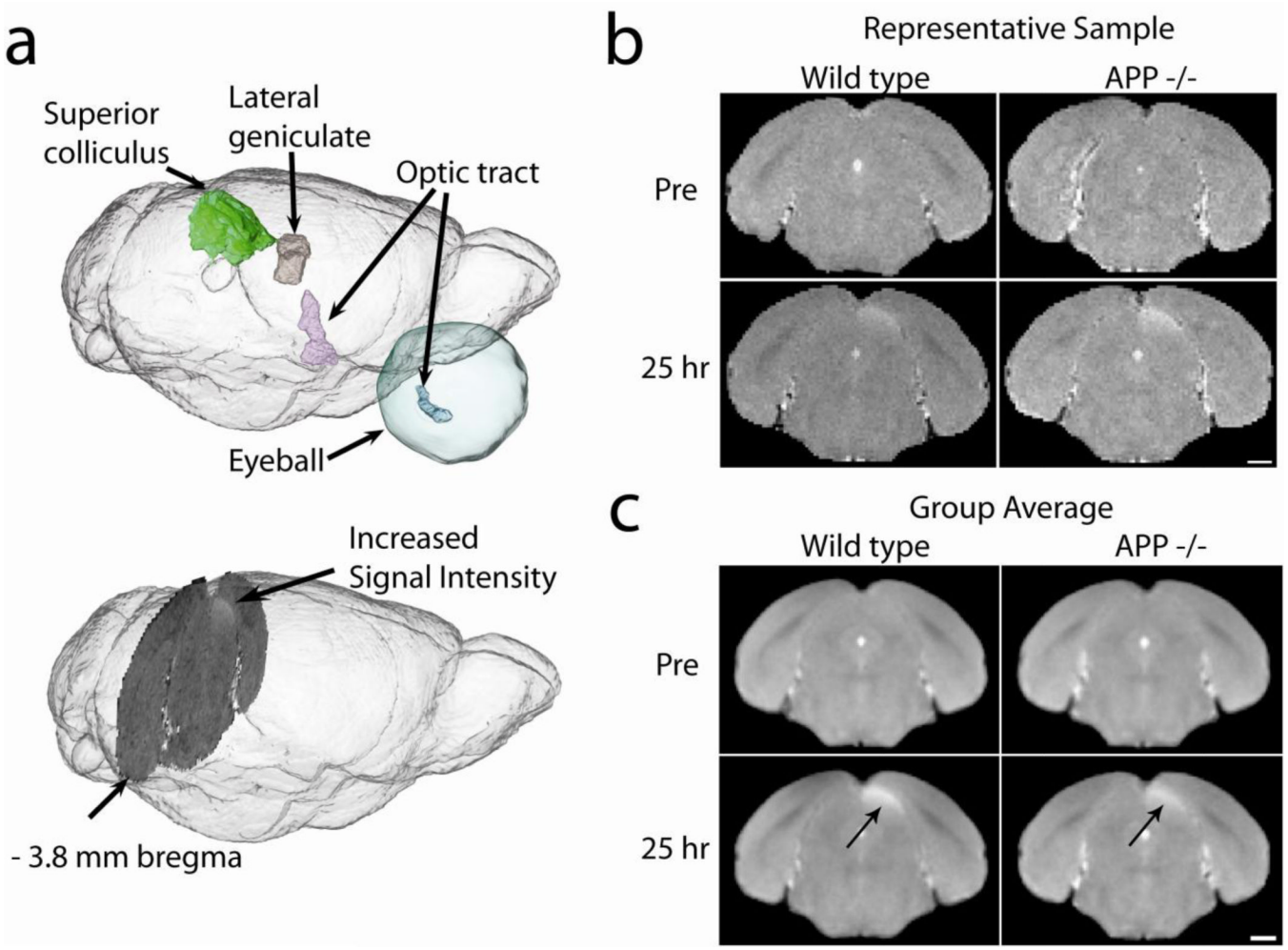

Figure 6. Representative and group average time-lapse coronal MR images demonstrate Mn^{2+} signal enhancement 25 hours after intra-ocular administration

(a) To aid visualization of Mn^{2+} transport following intra-ocular administration a rendering of the template surface with the superior colliculus structure (green), lateral geniculate (brown), internal optic tract (light purple), external optic tract (cyan) and eyeball (cyan) identified is presented. A single coronal MR slice (approx. bregma −3.8 mm) from a representative wild type mouse obtained 25 hours after injection demonstrates signal increases in the superior colliculus due to Mn^{2+} transport along the optic tract. (b) and (c) Representative and group average time-lapse MR coronal and axial images following intra-ocular Mn^{2+} administration for both groups; images obtained prior to (pre) and 25 hours (25 hr) after Mn^{2+} administration are presented. Visual inspection identifies an increase in the superior colliculus (denoted by arrows) at 25 hours due to transport of Mn^{2+} (Scale bar = 1 mm).

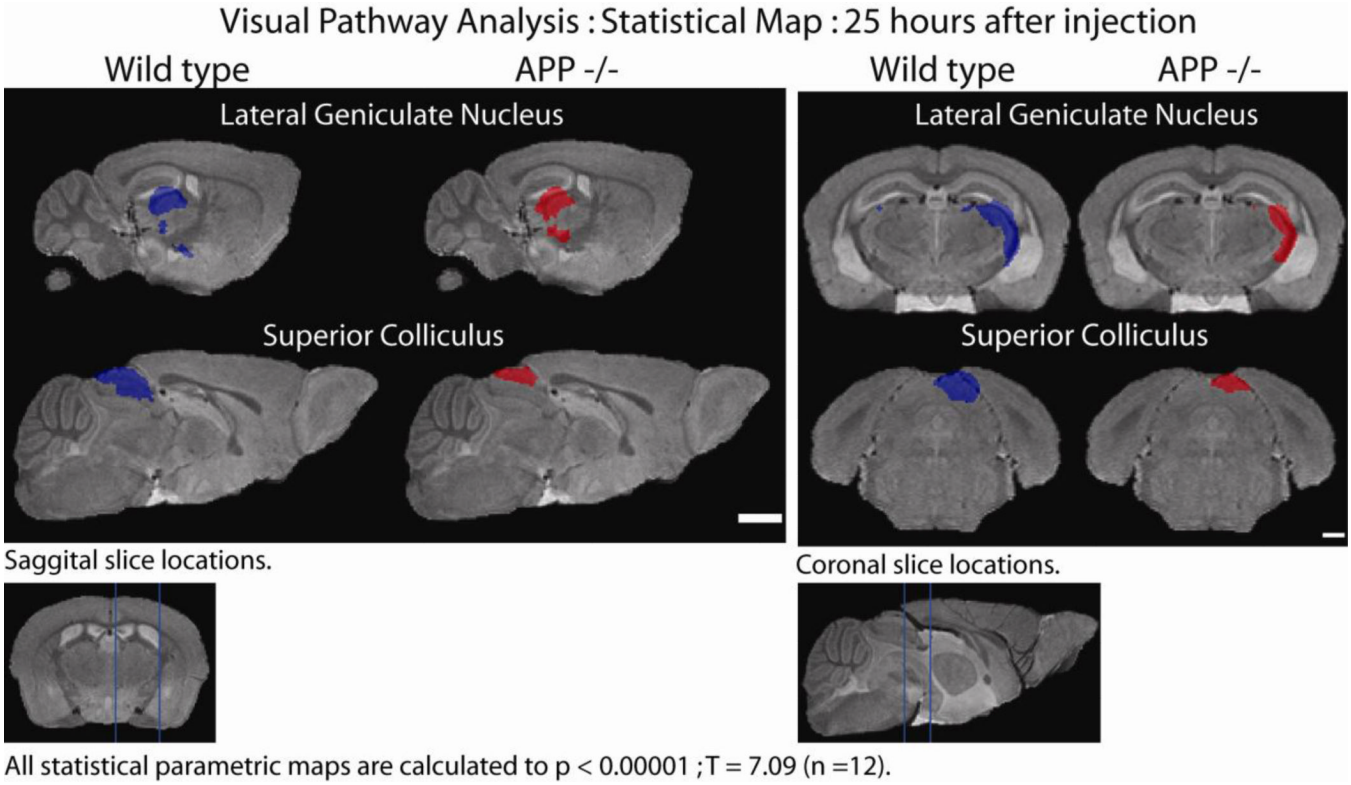

Figure 7. Mn^{2+} transport in the visual system is reduced in APP −/− mice

Statistical parametric analysis illustrating the statistically significant signal increase 25 hours after intra-ocular administration of Mn^{2+} in the structures along visual pathway for wild type mice (blue) and APP −/− (red) are presented. Maps are overlaid onto saggital and coronal images from the template (scale bar = 1 mm) to allow inspection of the changes at the lateral geniculate nucleus and superior colliculus; saggital images are positioned from midline at +2.40 mm and +0.44 mm respectively; coronal images are positioned at −2.30 mm and −3.88 mm bregma respectively. All statistical parameter maps are calculated to $p < 0.00001$ ($T = 7.09$; $n = 12$).

Table 1

Quantification of hippocampal and visual system increases.

	Hippocampal Injection Analysis						Visual System Analysis		
Time point	**1hr**		**7hr**		**25hr**			**25 hr**	
Genotype	**Wild type**	**APP −/−**	**Wild type**	**APP −/−**	**Wild type**	**APP −/−**		**Wild type**	**APP −/−**
Ipsilateral Hippocampus	0.93 (7.5%)	0.84 (6.8 %)	6.35 (51.3 %)	7.67 (61.9 %)	4.74 (38.3 %)	3.50 (28.3 %)	**Lateral geniculate nucleus**	0.43 (26 %)	0.28 (17%)
Contralateral Hippocampus	0 (0%)	0 (0%)	0 (0%)	0 (0%)	3.02 (23.8 %)	0.25 (1.9 %)	**Superior colliculus**	1.81 (16 %)	0.90 (6 %)
Septal Nuclei	0 (%)	0 (0%)	0.39 (17.6%)	0.11 (5.14 %)	1.01 (45.2 %)	0 (0 %)			
Ipsilateral Amygdala	0 (0 %)	0 (0%)	0.17 (8.5 %)	0 (0%)	1.16 (56.4%)	0.33 (5.9 %)			

Data are presented in cubic mm; the percentage of the respective anatomical region covered is in brackets.